Numerical Study of Boundary-Layer Receptivity on Blunt Compression-Cones in Mach-6 Flow with Localized Freestream Hot-Spot Perturbations

Yuet Huang[1] and Xiaolin Zhong[2]
Mechanical and Aerospace Engineering Department, University of California, Los Angeles, CA 90095, USA

huangyuet@gmail.com

This paper presents the numerical simulations of transient flow under the effect of interaction between freestream hotspot perturbation and bow-shock on Purdue's blunt compression cones in Mach-6 freestream by using shock-fitting method. The flow conditions that are used in the simulations are the same as Boeing/AFOSR Mach-6 Quiet tunnel (BAM6QT) in Purdue University, and the comparison of the simulation results with Purdue's laser-spot wind-tunnel experiment results is expected. The geometric design of the blunt compression cones creates an adverse pressure gradient along the cone wall in streamwise direction, hence, the laminar-turbulence transition takes place at a shorter streamwise distance when comparing to the blunt straight-cones. The simulation results show that the hot-spot excites second mode instability, and the growth of it is found to be dominant in boundary layer at downstream. The results of numerical simulation are well compared with results of linear stability theory (LST).

I. Introduction

In the process of designing hypersonic aerospace vehicles, prediction of the boundary layer laminar-turbulence transition location on the body surface is very important for conducting aerodynamic heating analysis. In general, the process of laminar-turbulence transition can be divided into three stages: (i) boundary layer receptivity, (ii) linear eigenmode growth or transient growth, and (iii) nonlinear breakdown to turbulence [16]. Boundary layer receptivity is the process of freestream disturbances enter boundary layer and generate instability waves. It is the first stage for laminar-turbulence transition to occur [2, 8].

For hypersonic flow, the dominant boundary layer instability in downstream of leading edge is the normal mode waves. The unstable normal modes were extensively studied by Mack, who showed that the second mode was the dominant instability, which leads to transition when freestream Mach number is approximately higher than 4 [7, 19]. Therefore, for hypersonic boundary layer with weak freestream disturbances, the most likely transition path is due to the second mode instability. Hence, the boundary layer receptivity of linear disturbance waves and the development of second mode instability in boundary layer are particularly important to the study of hypersonic boundary layer transition.

In hypersonic flow over a blunt body, the bow-shock in front of the body creates an entropy and vorticity layer, and these layers are eventually swallowed by the boundary layer in downstream [8]. It has been argued by many researchers that the swallowing process of entropy layer has a strong effect on the boundary layer stability [7]. Thus, the second mode instability can be affected by the entropy layer swallowing process [7].

Kovasznay [11] stated that weak disturbances in compressible flow can be decomposed into acoustic, entropy and vorticity disturbance. It was found that regardless of the type of freestream disturbances before hitting the bow shock, acoustic, entropy and vorticity disturbances would always be generated behind the

[1] Doctorate Student, Mechanical and Aerospace Engineering Department, AIAA Member.
[2] Professor, Mechanical and Aerospace Engineering Department, AIAA Associate Fellow.

shock by the interaction between the freestream disturbances and the shock [10]. However, the mechanisms of the interaction of various types of freestream disturbance with the shock are individually different, leading to difference in wave angles and amplitudes of the generated disturbances. In reality, the disturbances existing in the freestream during flight in atmosphere consist of all three kinds. Thus, detailed boundary layer receptivity studies for all three types of freestream disturbance are necessary for understanding the mechanism of hypersonic boundary layer receptivity over blunt bodies. Studies of hypersonic boundary layer receptivity to freestream acoustic disturbance have been conducted by many researchers [3, 4], and using a laser to generate hotspot is a practical way for imposing freestream disturbances other than acoustic disturbance in a wind tunnel [3, 4]. These are the reasons for researchers to conduct receptivity experiment with freestream hotspot perturbations.

The simulations in this paper are cooperated with the experiments at Purdue University. The schematic explanation of the laser-spot and cone setup in the previous experimental studies at Purdue University is demonstrated in Figure 1 [9, 32]. The hotspot was initially generated at a location upstream from the cone on the centerline. Then the spot convected with the hypersonic freestream toward the cone nose, and eventually interacted with and passed through the bow shock, and travelled further downstream in the shock layer above the cone.

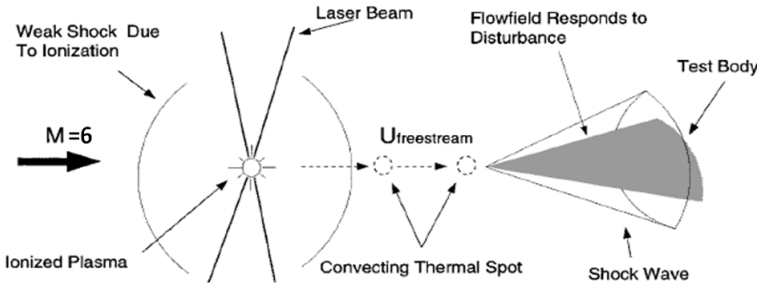

Figure 1. Schematic explanation of the laser-spot and cone scenario. [9]

Compression cone (see Figure 2) is a circular-base cone with circular-flared geometry along its body in downstream direction. Such geometry was expected to cause laminar-turbulence transition under quiet-flow condition due to adverse pressure gradient occurs along the flared geometry of the cone [5, 7]. The adverse pressure gradient is verified in Huang and Zhong's [13] mean flow numerical simulation, see Figure 3. The aim of having such geometry is to make the boundary layer thickness remain constant in downstream direction, while a narrow range of instability frequencies can be continuously amplified [5].

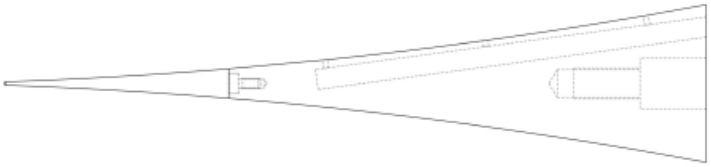

Figure 2. Schematic diagram of Purdue's Compression Cone [5]

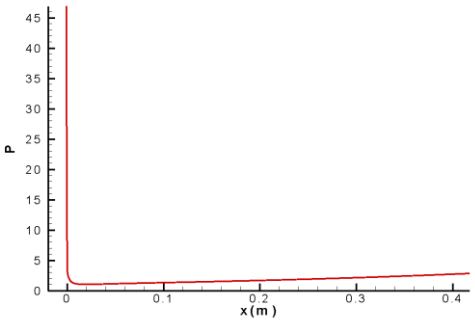

Figure 3. Pressure along the wall in case 2. [13]

In Huang and Zhong's [13] hotspot numerical simulation study in 2010, the results indicate that the freestream entropy perturbation would generate entropy and acoustic disturbances after passing through the bow shock. The results also show that the acoustic disturbance behind the bow-shock would bounce back from the wall and interact with the bow shock again, and generate acoustic and entropy disturbances.

Ma and Zhong [16] performed numerical simulation study on flat plate with freestream sinusoidal acoustic, entropy and vorticity waves at Mach-4.5. Ma and Zhong found that the receptivity of supersonic boundary layer to freestream entropy waves was essentially similar to that to freestream fast acoustic waves. Ma and Zhong also found that when the acoustic waves, which are generated from freestream entropy perturbation and shock interaction reached the boundary layer, the perturbed boundary layer would reflect the acoustic waves, and these waves would interact with the shock. This secondary acoustic wave and shock interaction would generate additional acoustic, entropy and vorticity disturbances. When these additional disturbances combined with the initial disturbances, they would produce strong effect on the boundary layer receptivity. For linear interaction of freestream waves with the shock, Ma and Zhong compared their simulation results with McKenzie et al. [10]'s theoretical results, and had a good agreement.

In 2010, Huang and Zhong [13] completed mean flow numerical simulation with shock-fitting method for a very blunt compression cone with nose radius of 0.0127m, and a sharper cone with nose radius of 0.001m. In order to validate the resulting mean flow, LST analysis was performed for the sharper cone mean flow, which gives N-factor = 12.5 with the most amplified frequency of 278996 Hz. Both LST and shock-front position results agree well with Purdue's shock-capturing numerical simulation results. Huang and Zhong developed the computer program for simulating the three dimensional hotspot perturbed flow behind bow-shock. They investigated the flow structure of the hotspot perturbation behind the bow-shock by computing two cases of freestream hotspots with very small radii.

This paper is a continuation of the realistic sized hotspot case numerical simulation from Huang and Zhong [13]. Since in that paper, the main focus is on creating the mean flow results, development and validations of the hotspot perturbed flow simulation computer code. In this paper, the goals are: (i) simulation of the unsteady hotspot perturbed flow for the entire blunt compression cone, (ii) the detailed investigations on instability modes excitation of hotspot perturbed boundary layer, which is performed after the simulation is completed.

II. Governing Equations and Numerical Methods

The governing equations for numerical simulation of hypersonic perfect-gas flow around compression cone are the following three-dimensional Navier-Stokes equations in conservative-law form and Cartesian coordinates:

$$\frac{\partial U}{\partial t}+\frac{\partial F_j}{\partial x_j}+\frac{\partial F_{vj}}{\partial x_j}=0,\ \ j=1,2,3 \tag{1}$$

The tensor notation, (x_1, x_2, x_3) represents the Cartesian coordinates, (x, y, z). x is the axis along the centerline of the cone, pointing in the direction from nose to bottom of the cone. y is the axis pointing vertically upward from the centerline of the cone, and it is perpendicular to the x axis. z is the axis perpendicular to both x and y axes, and it is pointing away from the centerline of the cone. The origin of the axes is at the center of origin of the spherical cone nose. Vector U contains five conservative-law form dimensional flow variables:

$$U=\begin{bmatrix}\rho & \rho u_1 & \rho u_2 & \rho u_3 & e\end{bmatrix} \tag{2}$$

where u_1, u_2, u_3 are velocity components, e is total energy per unit volume, ρ is mass density. Here, F_j and F_{vj} are the vectors of convective (invicid) flux and viscous flux in j^{th} spatial direction respectively:

$$F_j=\begin{bmatrix}\rho u_j\\ \rho u_1 u_j+p\delta_{1j}\\ \rho u_2 u_j+p\delta_{2j}\\ \rho u_3 u_j+p\delta_{3j}\\ (e+p)u_j\end{bmatrix} \tag{3}$$

$$F_{vj}=\begin{bmatrix}0\\ -\tau_{1j}\\ -\tau_{2j}\\ -\tau_{3j}\\ -\tau_{jk}u_k-q_j\end{bmatrix},\ \ k=1,2,3 \tag{4}$$

where P is the pressure, τ_{ij} is the shear stress tensor, and q_j is the heat flux due to thermal conduction.

The equation of the state and the transport equations are:

$$p=\rho RT \tag{5}$$

$$e=\rho\left(c_v T+\frac{1}{2}u_k u_k\right) \tag{6}$$

$$\tau_{ij}=\mu\left(\frac{\partial u_i}{\partial x_j}+\frac{\partial u_j}{\partial x_i}\right)-\lambda\frac{\partial u_k}{\partial x_k}\delta_{ij},\ \ \lambda=\frac{2}{3}\mu \tag{7}$$

$$q_j = -\kappa \frac{\partial T}{\partial x_j} \tag{8}$$

where R is the gas constant, T is the temperature, c_v is the specific heats that are assumed to be constant with a given specific heat ratio γ. κ is the heat conductivity coefficient, which can be determined with a constant Prantl number. The viscosity coefficient μ is defined by the Sutherland's law:

$$\mu = \mu_r \left(\frac{T}{T_0} \right)^{\frac{3}{2}} \left(\frac{T_r + T_s}{T + T_s} \right) \tag{9}$$

where μ_r is the reference viscosity coefficient, T_r is the reference temperature, and T_s is the Sutherland's temperature.

Throughout the numerical methods implementation in numerical simulation of hypersonic flow around the blunt compression cone, the Cartesian Navier-Stoke's equations have been transformed into body-fitted curvilinear computational domain coordinates (ξ, η, ζ) via Jacobian matrix. The computational domain is bounded by the bow-shock and the wall of the cone, which is called 'shock-fitting' domain. Using shock-fitting method can accurately resolve the position of the bow-shock, which is necessary to obtain the high accuracy of the flow solutions for receptivity and stability analyses. The shock-fitting grids are moving-grids in time, and the motion is depended on the shock position and the shock velocity. See Figure 4 for a partial view of grid configuration. In each time-step, shock position and shock velocity are the unknowns, and would be solved by the freestream conditions and behind-shock solutions. Spatial discretization of inviscid flux derivatives in stream-wise (ξ) and wall-normal (η) directions are done by using fifth-order finite-difference upwind schemes with local Lax-Friedrichs flux-splitting scheme, and sixth-order central finite-difference scheme is used for viscous flux spatial derivatives. For spatial derivatives in periodic azimuthal direction (ζ), Fourier collocation method has been used. Runge-Kutta method is used for time-marching. The details of shock-fitting method, finite difference schemes and other numerical method implementations of the numerical simulation are explained in Zhong's paper [6].

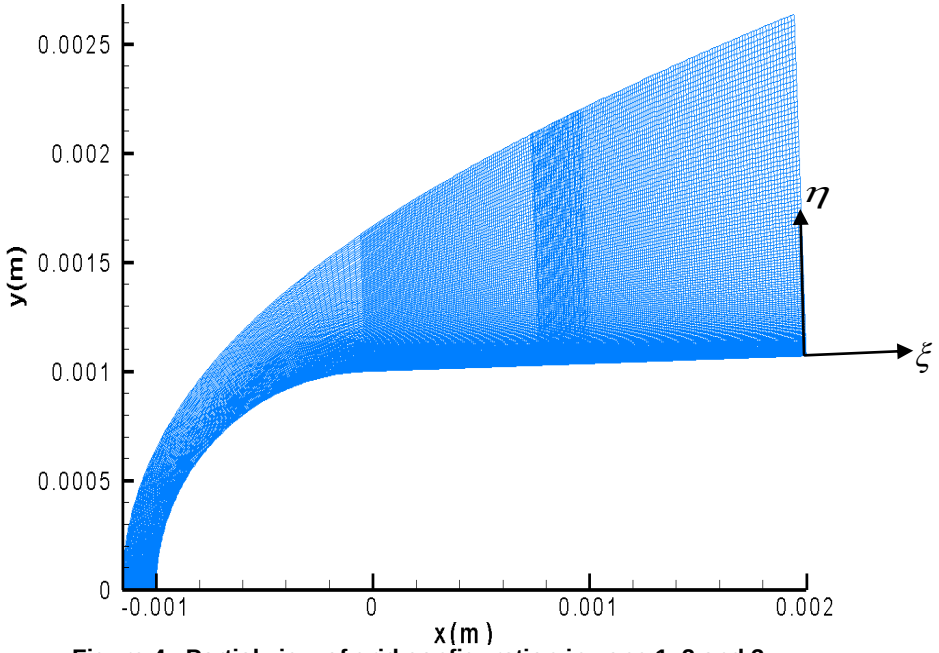

Figure 4. Partial view of grid configuration in zone 1, 2 and 3.

III. Modeling Equations of Freestream Hotspot Perturbations

In order to simulate the receptivity of boundary layer to freestream entropy spot, it is necessary to use a model for the implementation of the entropy spot in the simulation. In experiments, the hotspot is generated by laser in the freestream. In reality, a hotspot is an entropy perturbation sphere surrounded by weak acoustic perturbations. The core of the entropy has an approximately Gaussian temperature and density distribution [3, 4, 9, 32]. According to the experimental studies of hotspot [3, 4, 9, 32], the entropy perturbations are the dominant part of the hotspot perturbations, while the acoustic perturbations are very weak. Therefore, a simplified hotspot model of Gaussian entropy perturbations is used in the current numerical simulation study. This model contains most of the critical features of a hotspot, and it is easy to implement numerically.

For 3D hotspot model, the Gaussian perturbed freestream temperature is:

$$T = \Delta T_{\max} \exp\left(-\frac{R_c^2}{2\sigma^2}\right) + T_\infty \tag{10}$$

thus, by ideal gas law, the perturbed freestream density is:

$$\rho = \frac{p_\infty}{R\left(\Delta T_{\max} \exp\left(-\frac{R_c^2}{2\sigma^2}\right) + T_\infty\right)} \tag{11}$$

the time derivative of perturbed freestream density at shock location is:

$$\frac{\partial \rho}{\partial \tau} = \left(\frac{p_\infty}{\sigma^2 R} \right) T^{-2} \left(T - T_\infty \right) \left[\left(X_c - U_\infty t \right) \left(\frac{\partial X_c}{\partial \tau} - U_\infty \right) + y_{shk} \frac{\partial y_{shk}}{\partial \tau} + z_{shk} \frac{\partial z_{shk}}{\partial \tau} \right] \quad (12)$$

where σ is Gaussian shaping factor, τ is time in computational domain. X_{spot} is the initial x-coordinate of spot center. The initial x-coordinate difference between the shock location and the spot center is:

$$X_c = \left| X_{spot} - x_{shk} \right| \quad (13)$$

x_{shk}, y_{shk}, z_{shk} are shock-front coordinates. By using the transport equation in mathematics, the distance between hotspot center and any point on the shock front at any time is:

$$R_c = \sqrt{\left(X_c - U_\infty t \right)^2 + y_{shk}^2 + z_{shk}^2} \quad (14)$$

Please note that the time in computational domain is the same as the time in physical domain [6].

IV. Boundary Layer Instability Spectral Analysis

In the simulated result, the perturbations induced by the hotspot travelling along the cone surface contain a wide range of frequencies. In order to study the instability of the wave components of each individual frequency, we perform temporal Fourier spectrum analysis on the perturbation flow variables. By definition, continuous Fourier transformation of a flow variable *h(t)* is defined as [20]:

$$H(f) = \int_{-\infty}^{\infty} h(t) e^{2\pi i f t} dt \quad (15)$$

where *h(t)* is the flow variable time function, *H(f)* is its spectral value in frequency domain. Numerically, the continuous Fourier transformed spectral value can be approximated by:

$$H(f_n) \approx \Delta t \sum_{k=0}^{N-1} h_k e^{\frac{2\pi i k n}{N}} \quad (16)$$

where $H(f_n)$ is the spectral value at nth discretized frequency, N is the total number of Fourier collocation points used to discretize the time function, *h(t)*. The discretized time function is h_k. The spectral value, *H(f)*, has real and imaginary components in frequency domain. The $|H(f)|$ is the magnitude of the real part and the imaginary part of *H(f)*. In this paper, *h(t)* is the time-history of boundary layer perturbation, and the *H(f)* is the spectral value of the boundary layer perturbation in frequency domain.

After obtaining the frequency component of the boundary layer, it is necessary to validate the results of the numerical simulation. Here, the comparison with LST is chosen as a method to prove the validity of numerical simulation. In other papers, such as Zhong [7] and Sivasubramanian [21], the common practice is to compare the local spatial growth rate, local wave number, and the wall-normal boundary layer mode shape with LST.

Local growth rate in linear stability theory (LST) is defined as [19]:

$$\alpha_i = \frac{1}{\left|H(f_n)\right|}\frac{d\left|H(f_n)\right|}{ds} \tag{17}$$

where *s* is the natural coordinate along the body surface. Local wave number in LST is defined as [19]:

$$\alpha_r = \frac{d\varphi_n}{ds} \tag{18}$$

where φ_n is the phase angle of *H(f)* at nth discretized frequency. The wall-normal mode shape is the spatial distribution of the Fourier transformed spectral value, *H(f)*, along the normal of cone surface.

V. Freestream Conditions and Compression Cone Geometries

The freestream conditions that are used in the current numerical simulation are based on those of the Mach-6 Quiet Tunnel (BAM6QT) at Purdue University [5]. The flow is air and is assumed to be perfect gas. The viscosity of the flow is determined by Sutherland's law. The cone that is placed in freestream has zero angle of attack. The flow around the cone is assumed to be axisymmetric. The wall of the cone is smooth and rigid, and is isothermal. The details of the freestream conditions are summarized in Table 1.

Table 1. Freestream conditions.

M_∞	6.0
ρ_∞	$0.0403\ kg/m^3$
T_∞	$52.8\ K$
T_o	$433.0\ K$
T_{wall}	$300.0\ K$
γ	1.4
Pr	0.72
R	$287.04\ N\cdot m/kg\cdot K$ (*air*)
μ_r	$1.7894\times10^{-5}\ kg/m\cdot s$ (*sea level*)
T_r	$288\ K$ *(sea level)*
T_s	$110.3333\ K$
$\frac{\mathrm{Re}_\infty}{L}$	$1.026\times10^{7}\ m^{-1}$

where '∞' indicates the freestream value, 'o' indicates the total condition.

The geometry of the blunt compression cone is the same as that used in the experimental studies by Wheaton et al. [5]. It consists of two parts: a spherical nose section followed by a flared section. The spherical nose of the cone is blunt with a small radius, 0.001 meters. The starting point of the flared surface is tangent to the spherical nose surface with an initial angle of 2 degrees. The flared geometry has a circular arc of 3.0 meters in radius. The total length of the cone, which measures from the tip of spherical nose to the base of the cone along the centerline, is 0.45 meters. The schematic of the blunt compression cone are illustrated in Figure 2, and the details of geometry are summarized in Table 2.

Table 2. Basic geometry of compression cones.

body-arc radius	3.0 *m*
starting half-angle	2.0 *degrees*
cone length	0.45 *m*
nose radius	0.001 *m*

VI. Simulation Results

Unless mentioned specifically, all flow variables shown in the figures are dimensionless, which are normalized by the corresponding freestream values, for example, T/T_∞, P/P_∞, ρ/ρ_∞, S/S_∞, u_i/u_∞, dT/T_∞, dP/P_∞, $d\rho/\rho_\infty$, dS/S_∞, du_i/u_∞, etc. For all contour plots, the upper boundary is the location of the shock, the lower boundary is the cone-wall, the left boundary is the flow inlet, and the right boundary is the flow exit. Since the cone is at zero degree angle of attack, only the upper half of the cone is demonstrated, and the lower half is the mirror image of the upper half due to axis-symmetry of the flow. Figure 4 shows the partial view of the computational grid structure around the cone. Due to the limiting computer power for computing a huge amount of grid points at once, the simulation is divided into 18 zones. Zone 1 is the computation domain in the stagnation region over the hemispherical cone nose, zone 2 to zone 18 is the computation domain in the compression region over the cone. For zone 1 to 5, each zone has grid resolution of 120×120. For zone 6 to 12, each zone has grid resolution of 240×120. Starting from zone 13, at $x=0.17$ m, the resolution in wall-normal direction is doubled, because the gradient in wall-normal direction become very large at this location, more grid points in wall-normal direction are needed to accurately resolve the flow field. Therefore, for zone 13 to 18, each zone has grid resolution of 240×240.

A. Unsteady flow Solution with Hotspot Perturbations in Freestream

The unsteady numerical simulation is performed by imposing a hotspot perturbation on the mean flow. The freestream hotspot interacts with the bow-shock while entering the shock-layer, then it convects into boundary layer. After the hotspot enters the boundary layer, it excites second mode waves in downstream.

The Gaussian modeling equations in equations (10) and (11) are used to model a three-dimensional freestream hotspot. In current study, axisymmetric flow field with the freestream hotspot that is initially aligned with the centerline of the cone is computed. The non-axisymmetric case with off-centered hotspot will be considered in the future study.

In this study, we mainly focus on a particular case with a hotspot core radius of 0.003 meters. The hotspot is initially placed at 0.02 meters upstream from the bow shock along the centerline of cone. The hotspot core radius is controlled by a dimensionless Gaussian factor, σ. In this particular case, the dimensionless Gaussian factor is 0.001. The parameters of freestream hotspot perturbation in this case are summarized in Table 3.

Table 3. Parameters of freestream hotspot perturbation.

σ	Hotspot radius (m)	$X_{spot}\ (\mathrm{m})$
0.001	0.003	0.02

In the numerical simulation, the mean flow is first obtained. The unsteady simulation is carried out first by imposing the hotspot into the freestream according to the equations (12) to (14). Then the subsequent development of the perturbation in boundary layer is simulated. In this paper, only the linear development of boundary layer perturbation is focused, thus the hotspot with very weak amplitude is imposed in the freestream. In order to keep the disturbance growth linear in the flow, the freestream maximum relative temperature perturbation amplitude at the center of hotspot, ε, is chosen to be:

$$\varepsilon = \frac{\Delta T_{\max}}{T_\infty} = 10^{-4} \tag{19}$$

The freestream temperature is 52.8 Kelvin, therefore, we obtain the maximum freestream temperature perturbation amplitude:

$$\Delta T_{\max} = T_\infty \times \varepsilon = 0.00528K \tag{20}$$

The parameters of the freestream hotspot perturbation in Table 3 are chosen based on the laser spot in experimental studies by Salyer et al. [3, 4]. By having the hotspot parameters in Table 3 and the maximum freestream temperature perturbation amplitude from equation (20), the freestream hotspot model can be successfully resolved by equations (10), (11), (13) and (14).

In the current simulation, the hotspot enters the shock layer after interacts with bow shock. It travels from the stagnation region over the nose of the cone into boundary layer in downstream. After the perturbations pass through the computation domain, the flow field returns to the mean flow state. Figure 5 and Figure 6 are the snapshots of pressure and entropy contours of hotspot perturbations in upstream region over the cone. The snapshots in upstream region are taken in zones 1, 2, 5 and 9. Figure 7 and Figure 8 are the snapshots of pressure and entropy contours of hotspot perturbations in middle region over the cone. The snapshots in middle region are taken in zones 12 and 14. Figure 9 and Figure 10 are the snapshots of pressure and entropy contours of hotspot perturbations in downstream region over the cone. The snapshots in downstream region are taken in zones 17 and 18. For each snapshot, we plot the moment when the hotspot perturbations travel from the left boundary to the right boundary in each zone.

The structures of hotspot perturbations in upstream region over the cone are demonstrated in Figure 5 and Figure 6. Zone 1, which is shown in Figure 5 (a) and Figure 6 (a), is the stagnation region of the hemispherical cone nose, where the hotspot first enters the shock layer. The core of pressure perturbation in Figure 5 (a) is at the stagnation point of the cone, and has the maximum absolute magnitude of the perturbation. The entropy perturbation in Figure 6 (a) has a core of maximum absolute magnitude appears at the stagnation line next to the bow shock. The hotspot enters the shock layer from freestream, and it travels towards right-hand-side. Eventually it passes through the right-most exit boundary and convects into the next zone, namely "zone 2." Zone 2, which is shown in Figure 5 (b) and Figure 6 (b), is the first zone behind the stagnation region, thus the effect of change in surface geometry is dominant in this zone. While the hotspot passing through zone 2, the pressure perturbation, which is acoustic in nature, hits the shock and reflects back towards the wall. However, entropy perturbation is convective, and it does not reflect from the wall. Zone 5 is shown in Figure 5 (c) and Figure 6 (c). The pressure perturbation in zone 5 has positive amplitude appears near the wall, but it has negative amplitude in zone 2 next to the wall. This phenomenon may be a result from the acoustic reflection of the pressure perturbation at the wall. In zone 5, part of the boundary layer entropy perturbation travels ahead of the main body of the hotspot outside the boundary layer. The rear part of the entropy is elongated. The appearance of such flow structure may be due to the viscous nature of boundary layer that causes different parts of the boundary layer perturbation travels at different velocities to the main body of the hotspot. Zone 9, which is shown in Figure 5 (d) and Figure 6 (d), spans a longer streamwise distance, thus the entire structure of hotspot in upstream region over the cone and its spatial evolution are clearly demonstrated. The pressure perturbation has acoustic wave in front of and behind the main body of hotspot. These waves could be the fast acoustic wave and slow acoustic wave respectively. The entropy perturbation that is ahead of the main hotspot body in previous zones travels even farther ahead of it. Moreover, the rear part of the entropy perturbation also becomes much longer, it eventually forms a tail and breaks apart from the main body of hotspot. The overall intensity of the entropy perturbation decays while travelling towards downstream. There are only decaying waves appeared, the modes that are contained in the

hotspot perturbation by zone 9 are spatially stable.

As the hotspot travels further into the middle region over the cone, the size of the hotspot is much expanded and its shape is much elongated, when compares to the hotspot in upstream region. The structures of hotspot perturbations in middle region over the cone are demonstrated in Figure 7 and Figure 8. However, the size of a zone is not large enough to demonstrate the entire hotspot in a single snapshot, hence there are several snapshots made to demonstrate the parts of the hotspot while it passing by a zone. Zone 12, which is shown in Figure 7 (a), (b) and Figure 8 (a), (b), is the zone right before the 'sensitive' region. 'Sensitive' here means a small perturbation here can easily trigger the instability of the flow. The pressure perturbation has two parts: the front part and the rear part. The front part is essentially the acoustic wave travels faster than the hotspot main body, and the rear part is essentially the acoustic wave that travels slower than the main body. Especially in the boundary layer, there are oscillations appear like some kinds of wave mode for both front and rear parts. The entropy perturbation has essentially two parts here, the main body and the first tail (in downstream, there will be another tail appeared). The boundary layer perturbations, which travel ahead of the main body, attenuate and become insignificant in zone 12. In zone 14, which is shown in Figure 7 (c), (d) and Figure 8 (c), (d), the pressure perturbation just keeps on decaying, and there is neither growth nor new mode is seen. The intensity of the main body of entropy perturbation decays so much. The first tail of entropy perturbation also decays, but not as much as the main body, so the intensity of the first tail becomes significant. Moreover, the first tail becomes oscillatory.

As the hotspot reaches the downstream region over the cone, the unstable waves appear as tails, which travel slower than the main body of the hotspot. The flow structures of hotspot perturbations in downstream region over the cone are demonstrated in Figure 9 and Figure 10. The pressure perturbation in zone 17 is demonstrated in Figure 9 (a), (b) and (c), the front part and the rear part of the main body grows slowly. Simultaneously, a spatially unstable tail appears behind the main body of pressure perturbation. The intensity of the tail is approximately the same order of magnitude to the main body of pressure perturbation. The tail appears in oscillatory form. It can be shown to be the unstable second mode, which will be verified in the latter part of this paper. The entropy perturbation in zone 17 is shown in Figure 10 (a), (b) and (c). The first tail in entropy perturbation is oscillatory. The first tail seems to be a neutral/unstable mode, since it does not decay but slightly grows spatially. Simultaneously, the second tail appears in zone 17. The intensity of the second tail grows vigorously while travelling further downstream. The pressure perturbation of zone 18 is demonstrated in Figure 9 (d), (e) and (f). The main body, which consists of front and rear parts, becomes subdominant while the tail growing to a level that exceeds the main body of hotspot pressure perturbation in zone 18. The entropy perturbation in zone 18 is shown in Figure 10 (d), (e) and (f). The main body of hotspot entropy perturbation keeps attenuating. The first tail grows at a slower rate than the second tail. The second tail grows to a level that dominates the perturbation. The first tail seems like a connection mode that connects between the stable main body and the unstable second tail. Both second tails of entropy perturbation in zone 17 and 18 are "rope" structured waves appear at the boundary layer thickness above the wall. The wavelengths of these rope waves are approximately twice of their boundary layer thicknesses. These are typical properties of second mode waves [50].

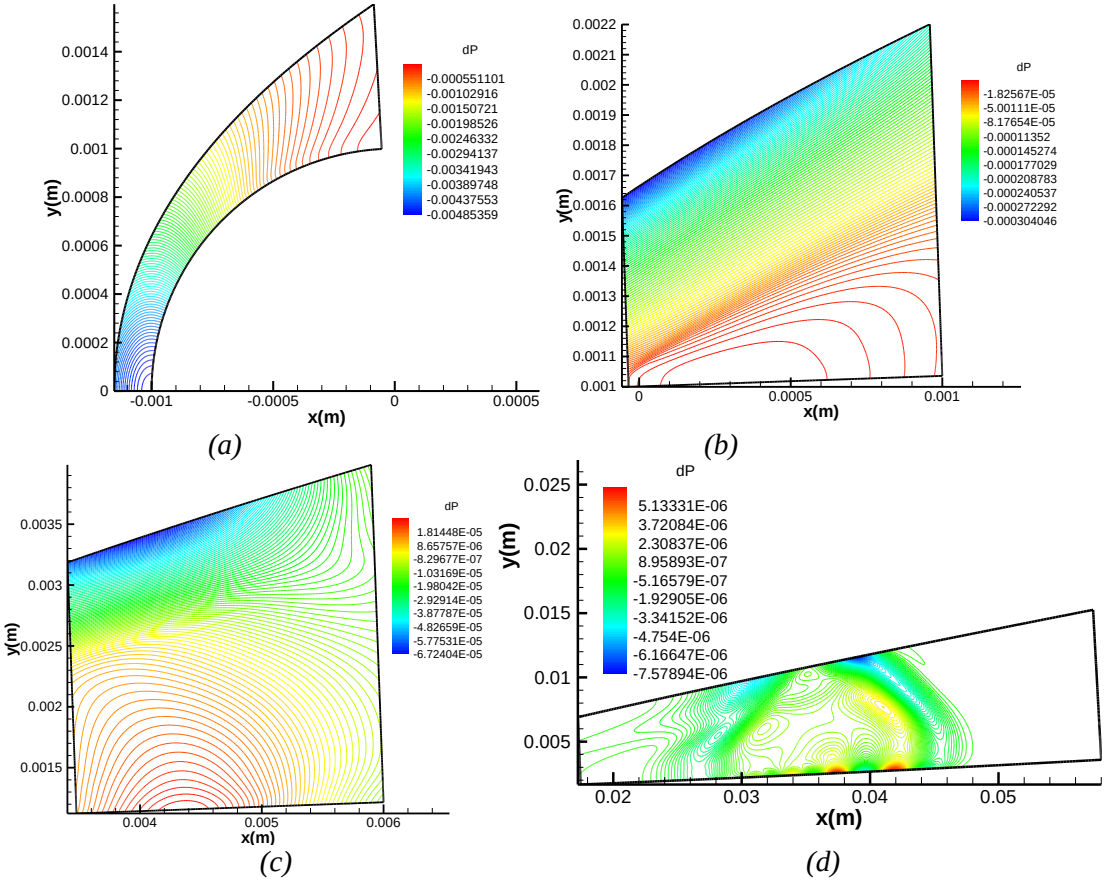

Figure 5. Contour plot of hotspot pressure perturbation behind the shock in upstream region over the compression cone: (a) in zone 1, (b) in zone 2, (c) in zone 5, (d) in zone 9.

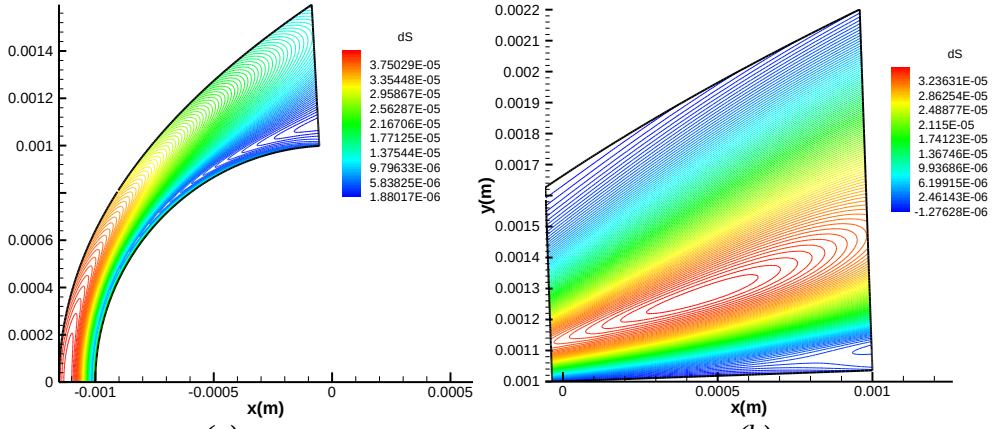

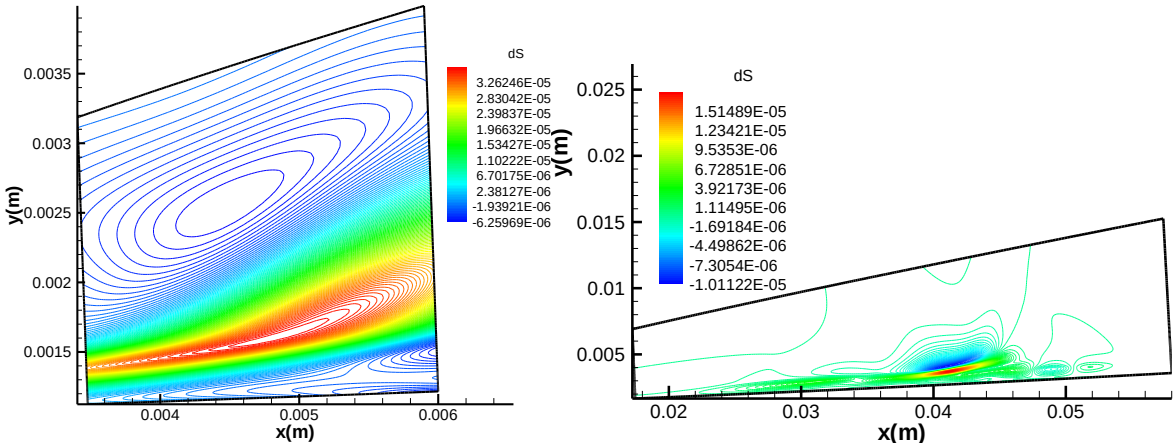

(c) *(d)*

Figure 6. Contour plot of hotspot entropy perturbation behind the shock in upstream region over the compression cone: (a) in zone 1, (b) in zone 2, (c) in zone 5, (d) in zone 9.

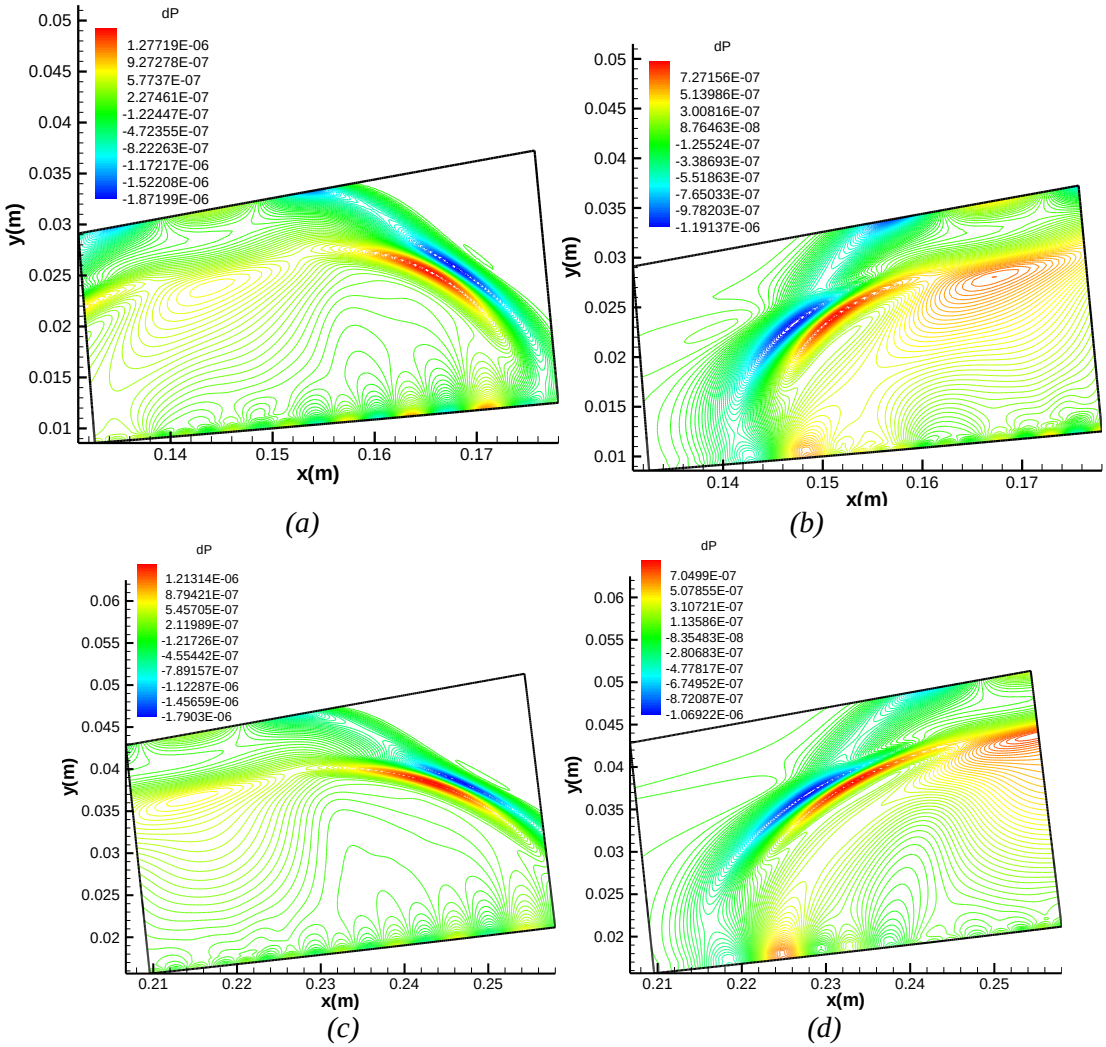

(a) *(b)*

(c) *(d)*

Figure 7. Contour plot of hotspot pressure perturbation in middle region over the compression cone: (a) the

front part in zone 12, (b) the rear part in zone 12, (c) the front part of in zone 14, (d) the rear part in zone 14.

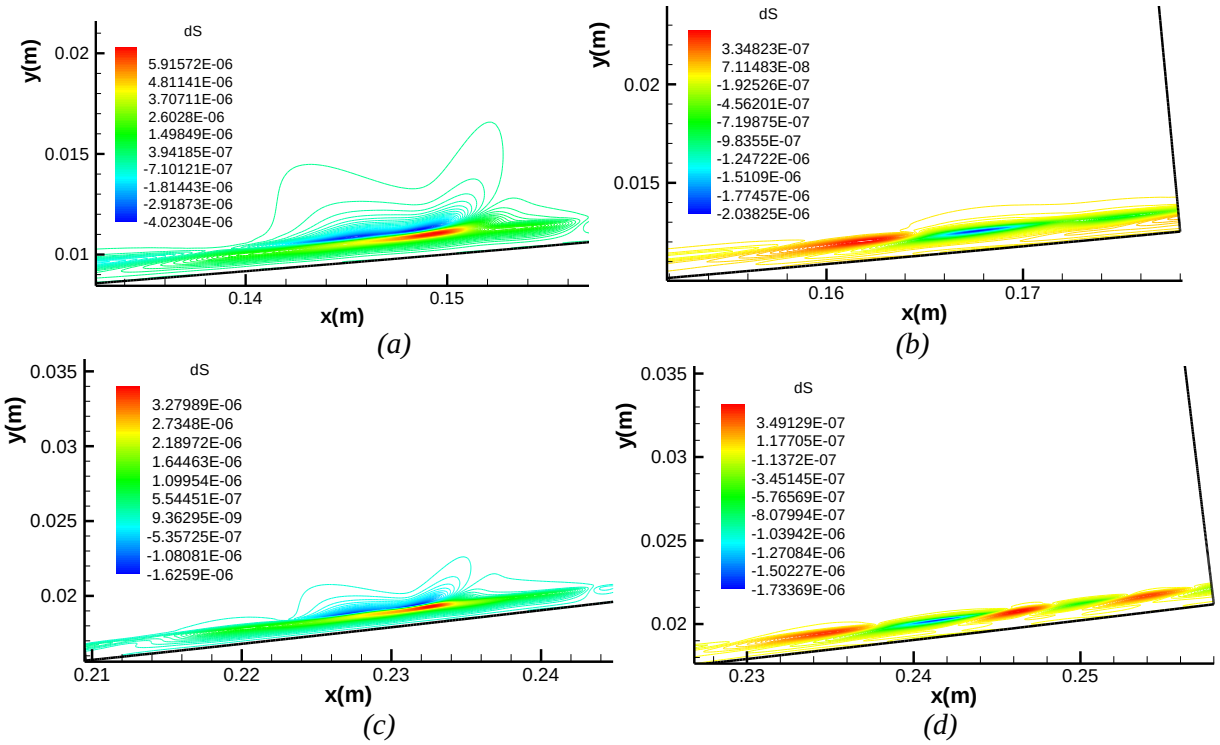

Figure 8. Contour plot of hotspot entropy perturbation in middle region over the compression cone: (a) the main body in zone 12, (b) the first tail in zone 12, (c) the main body in zone 14, (d) the first tail in zone 14.

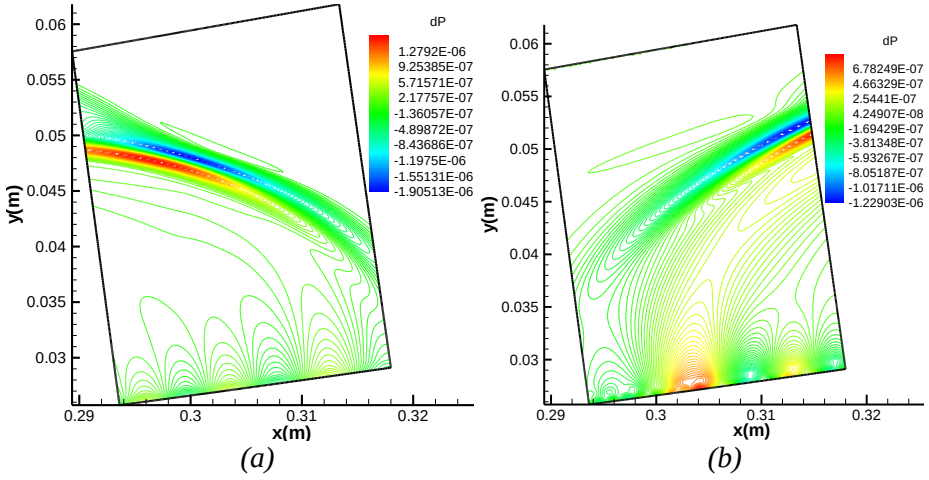

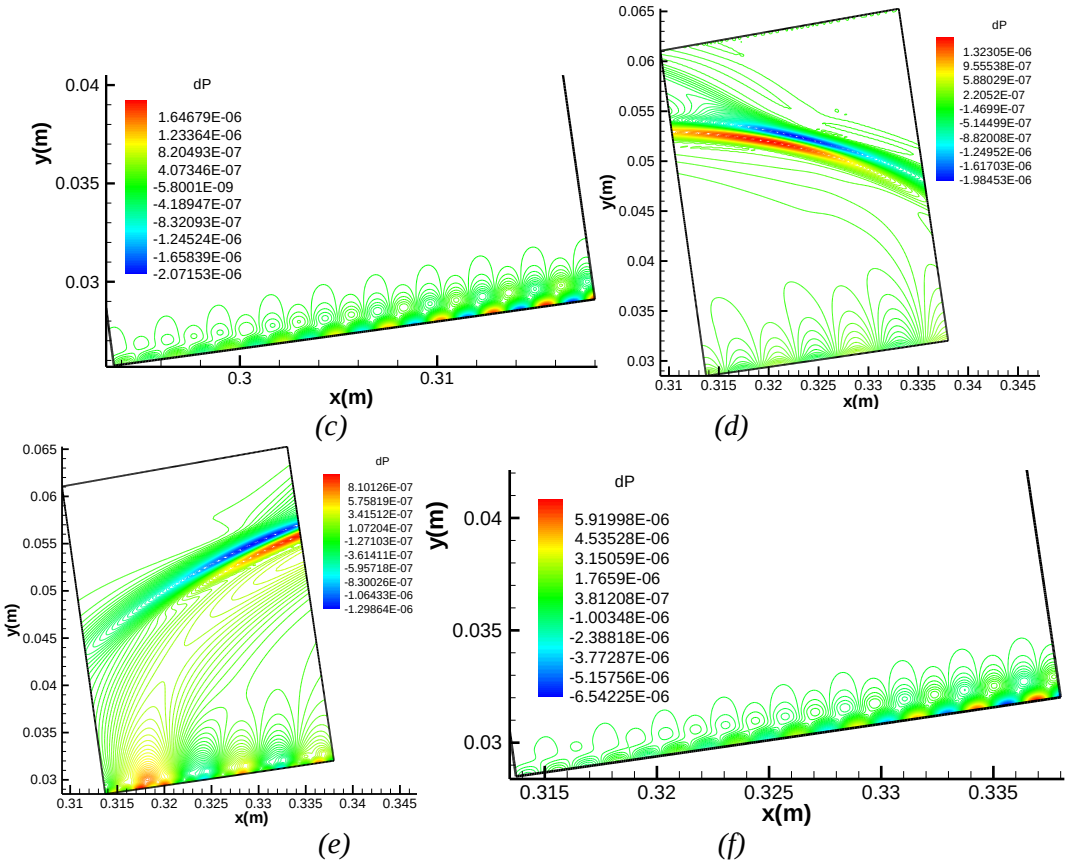

Figure 9. Contour plot of hotspot pressure perturbation in downstream region over the compression cone: (a) the front part in zone 17, (b) the rear part in zone 17, (c) the tail of in zone 17, (d) the front part in zone 18, (e) the rear part in zone 18, (f) the tail in zone 18.

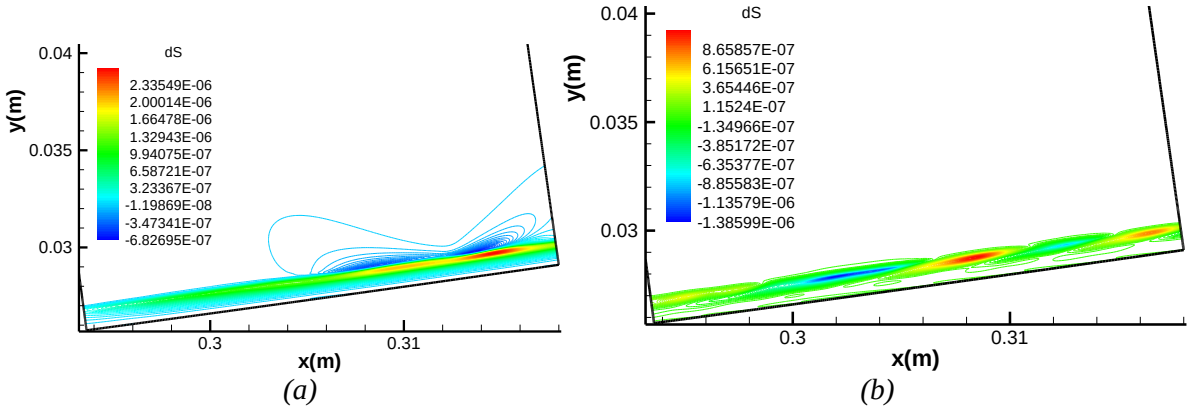

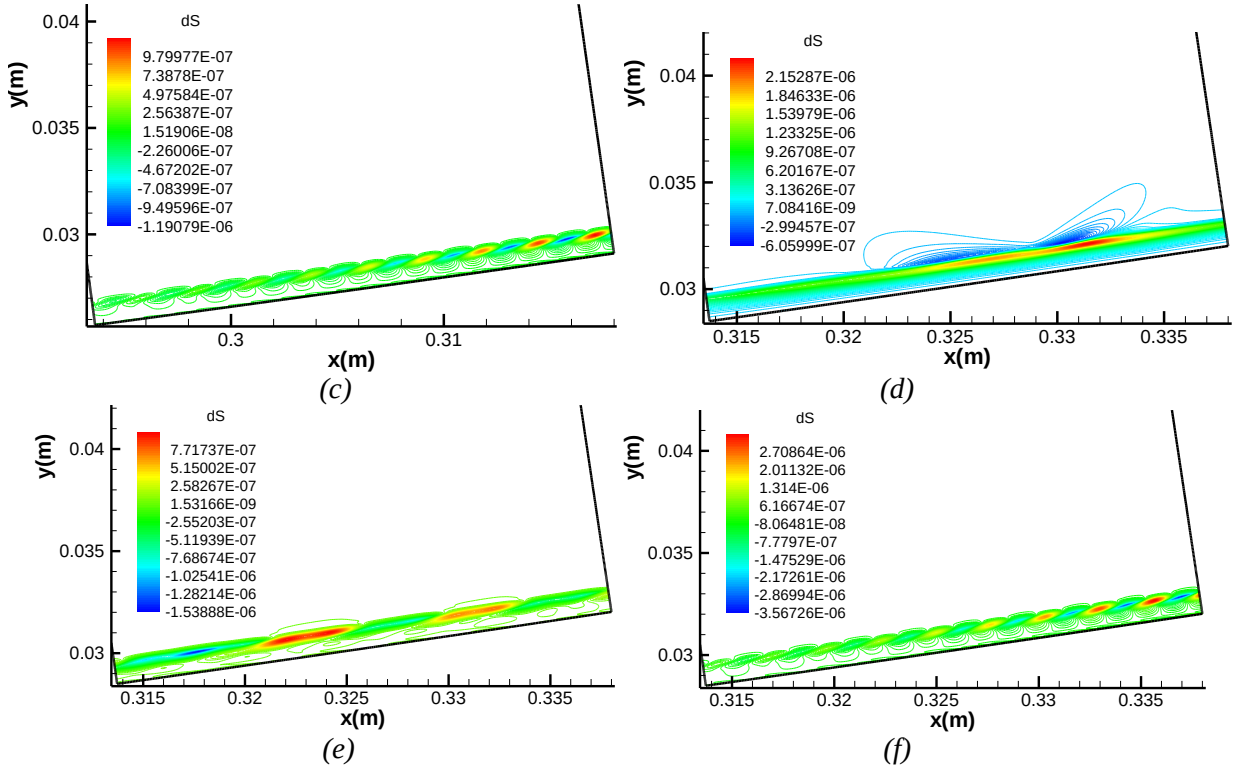

Figure 10. Contour plot of hotspot entropy perturbation in downstream region over the compression cone: (a) the main body in zone 17, (b) the first tail in zone 17, (c) the second tail in zone 17, (d) the main body in zone 18, (e) the first tail in zone 18, (f) the second tail in zone 18.

At this time, receptivity experiment measurements with freestream laser-spot are very limited. Therefore, it is not possible to have a quantitative comparison to the current numerical simulation results. The most comparable experimental measurement to the current numerical simulation results is the one done by Randall [22]. Randall's experiment is a laser perturbation receptivity experiment on a hemispherical nose in Mach 4 freestream. Figure 11 (a) is the wall pressure perturbation time-history profile of a laser spot near stagnation point of a hemispherical nose in Randall's Mach 4 experiment [22], which is also referenced by Ladoon et al. [28]. This wall pressure perturbation time-history profile has a very oscillatory shape originally, which is shown in dash line, so there is a solid line profile, which is the original profile filtered at 100 kHz. Figure 11 (b) is the numerically simulated hotspot wall pressure perturbation time-history profile at $x = 0.0135\ \mathrm{m}$, which is about 3% of the total cone length. Figure 11 (c) is the numerically simulated hotspot wall perturbation time-history profile at $x = 0.17\ \mathrm{m}$, which is about 38% of the total cone length. In Figure 11 (b), the hotspot profile at 3% of the total cone length can be considered as the profile very near the cone nose. Therefore, the shape of the hotspot profile is relatively monotonic, and it is unaltered by the evolution of different wave modes in boundary layer. The profile in Figure 11 (b) is quite comparable to the noise filtered shape of the experimental measured laser spot in Figure 11 (a). From the time-history profile at 38% of the cone length in Figure 11 (c), the profile is altered by the evolution of multi-wave modes in boundary layer, therefore it is oscillatory, but the growth of second mode is not encountered yet. The profile in Figure 11 (c) is qualitatively similar to the original noise unfiltered wall pressure perturbation profile in Figure 11 (a).

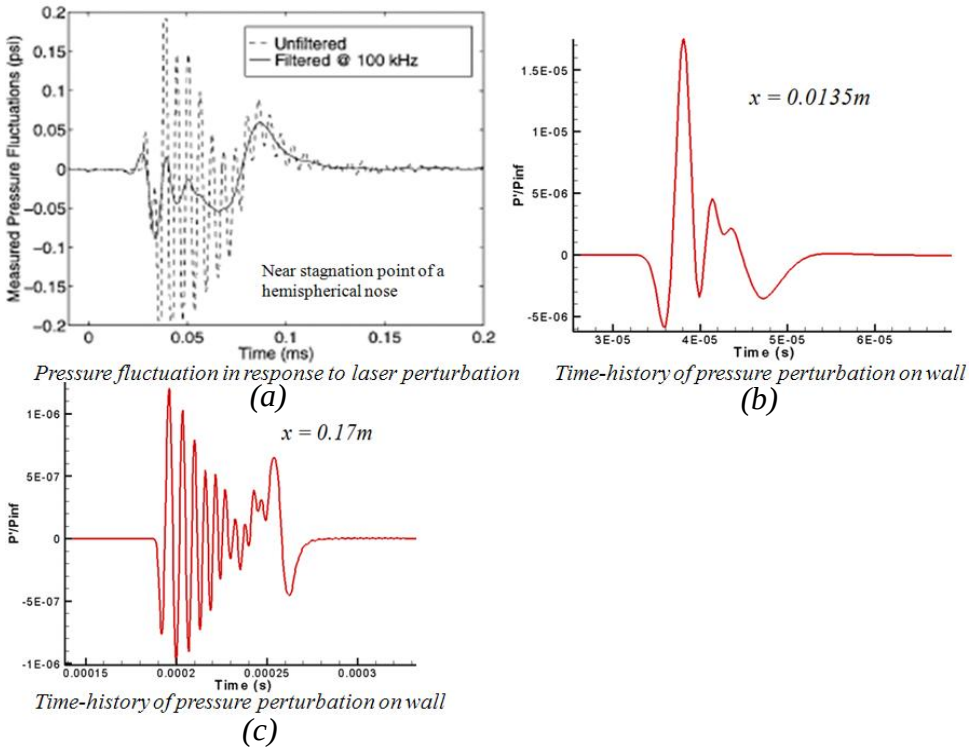

Figure 11. Comparisons of the wall pressure perturbation time-history profile between (a) the experiment by Randall [22, 28] and (b), (c) the current numerical simulation.

B. Boundary Layer Receptivity Analysis

The numerical solution for the time-history of the wall pressure perturbation is recorded at various spatial locations in the downstream direction. Figure 12 and Figure 13 are the plots of the time-history traces, where the wall pressure perturbation amplitude is normalized with respect to the freestream pressure. The earliest location for the wall pressure perturbation to arrive in the listed spatial range in each figure is the bottom plot, and the exit location of the listed spatial range is the plot at the top position.

The wall pressure perturbation first travels through the upstream part of the cone, and the corresponding time-history trace is shown in Figure 12. In the upstream part of the cone, the perturbation time-history profile starts with a relatively monotonic shape, which consists of a main peak and a lower peak. Both peaks could be fast acoustic wave and slow acoustic wave, and they gradually decay while travelling downstream, and split into a multi-peak shape.

After the wall pressure perturbation exiting the upstream part of the cone, it enters the downstream part of the cone, and the corresponding time-history trace is shown in Figure 13. In the downstream part of the cone, the multi-peak shaped perturbation begins to split into two parts in time: one with more oscillatory profile and the other one with a smoother profile. As it travel further downstream, the perturbation amplitude decays, and both parts depart from each other in time. Both parts are different wave modes, since they have totally different perturbation profile, and they travel with different velocities; the more oscillatory part travels faster than the smoother part. While the perturbation moving further downstream, another new perturbation mode appears, and its amplitude grows so rapidly. The new perturbation mode amplitude soon surpasses the original decaying modes and become the dominant instability in boundary layer. This new perturbation mode is the second mode instability, it appears in the time-history profile around $x = 0.25$ m, which is 56% of the

total cone length. At the same locations as the second mode wave appears, there is also a less dominant growing mode connecting the decaying modes and the dominantly growing second mode. Even though there is likelihood that this less dominant growing mode may be the first unstable mode wave, by taking the reciprocal of its period, the frequency of it is found to be 285 kHz, which falls in the frequency range of the second mode instability (the frequency range of second mode instability is presented in latter part of this paper). The farthest location in current numerical simulation is $x = 0.394\ \mathrm{m}$. At the farthest location, the time-history profile of the wall pressure perturbation is demonstrated in Figure 14. The relative magnitude of second mode pressure wave to the local mean flow pressure reaches $O\left(10^{-5}\right)$.

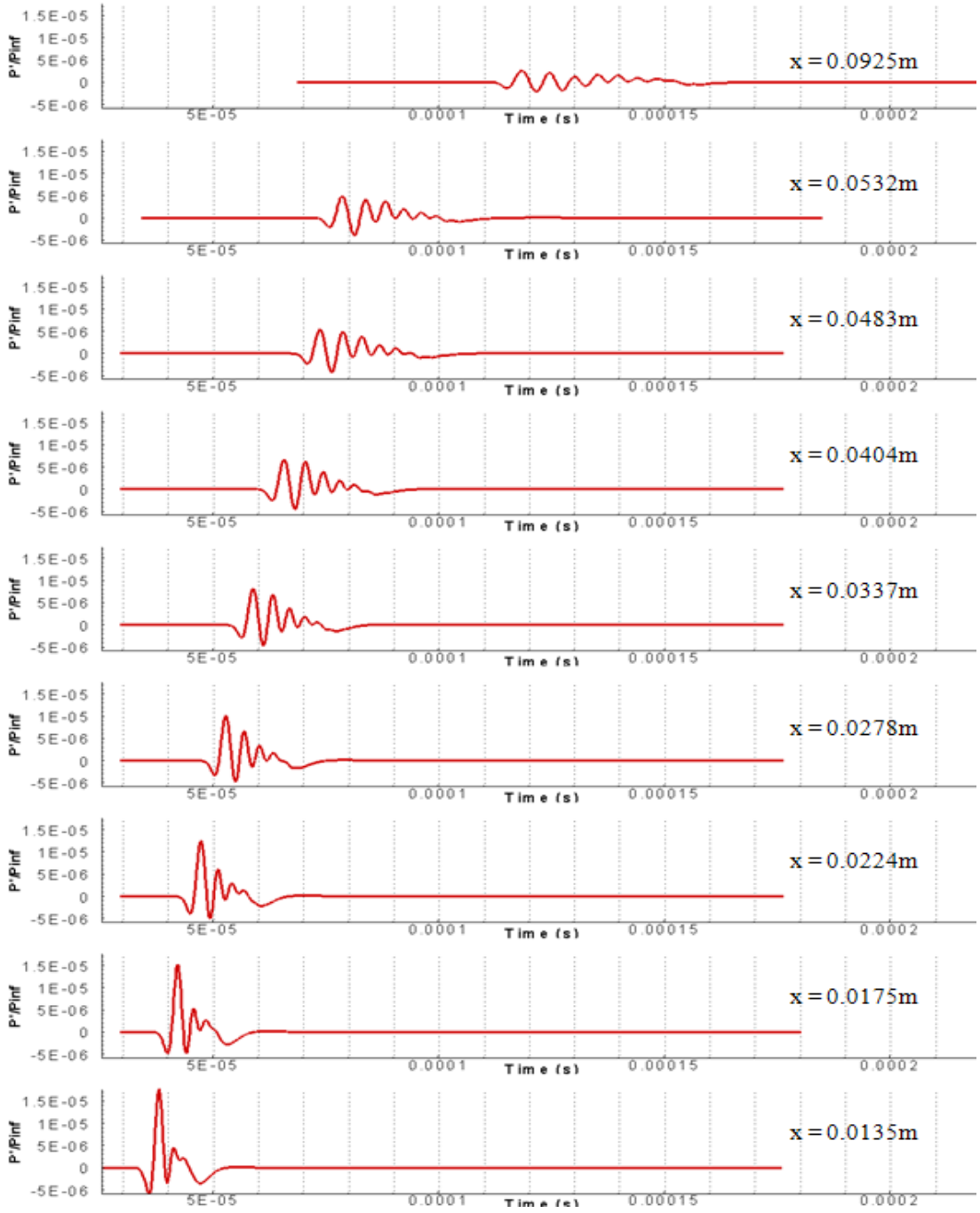

Figure 12. Time-history traces of pressure wall-perturbation at various streamwise locations at the upstream part of the cone.

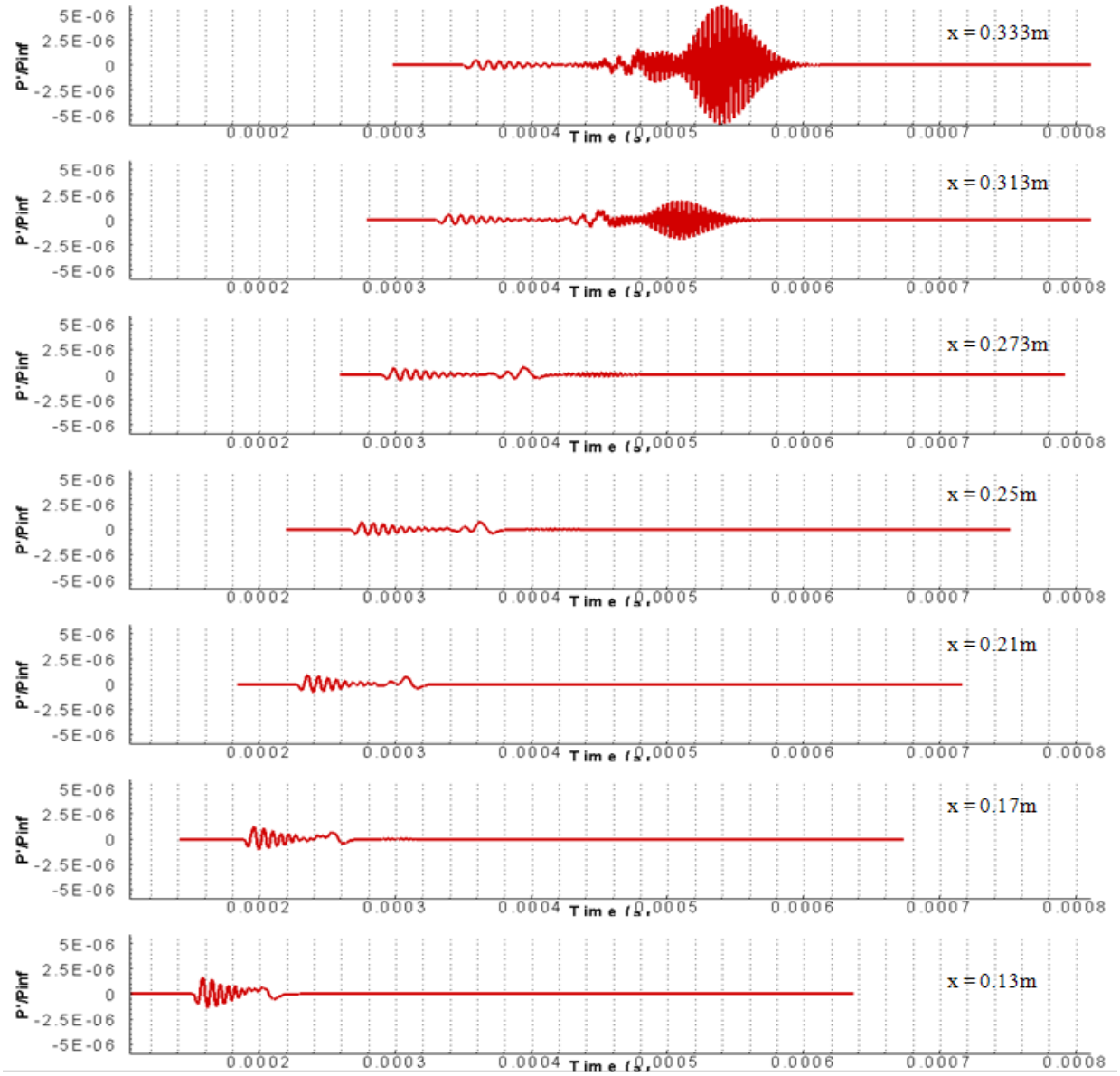

Figure 13. Time-history traces of pressure wall-perturbation at various streamwise locations at the downstream part of the cone.

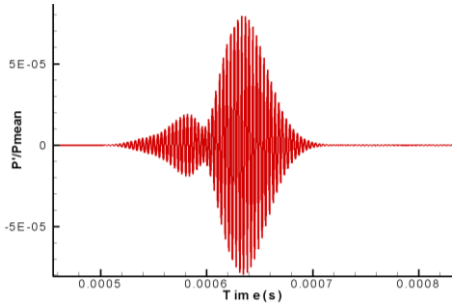

Figure 14. Time-history of wall-pressure perturbation relative to the local mean flow pressure at x=0.394 m.

In order to find out which component of the pressure causes boundary layer instability, further in-depth investigations of the wall pressure perturbation time-history are necessary. Fourier transformation based on the wall pressure perturbation time-history is taken at various locations to obtain the frequency spectrum of wall pressure perturbation, which is shown in Figure 15. Each curve in the plot represents different locations on the cone. The plot clearly shows that there is a spatially growing amplitude peak at the frequency range from about 260 kHz to 320 kHz. This growing peak is the second mode instability, which is verified in the latter part in this paper. The peak to the left of the growing peak, which is at the frequency range from 120 kHz to 240 kHz, decays spatially. This decaying peak could be the first mode wave at lower frequencies. There is also another spatial growing peak appears between 520 kHz and 600 kHz from $x = 0.374$ m to further downstream. This growing peak should be the second harmonic wave, since its frequency range is about twice of the second mode wave frequency range. The existence of second harmonic wave implies that there are nonlinear wave interactions in boundary layer begin from $x = 0.374$ m to further downstream.

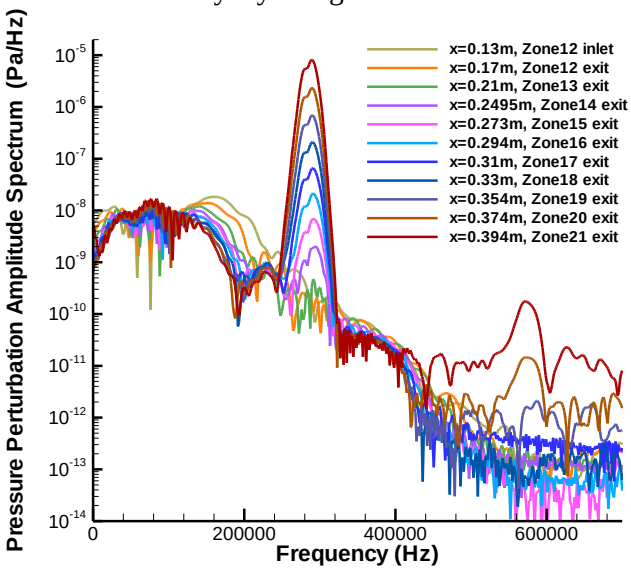

Figure 15. Dimensional frequency spectrum of wall pressure perturbation.

Freestream hotspot perturbation has a Gaussian temperature profile in time. By taking Fourier transformation of it, the frequency spectrum has also a Gaussian distribution, which is demonstrated in Figure 16. The Gaussian distributed frequency spectrum of freestream temperature perturbation has higher amplitude in lower frequencies, and the amplitude decays while increasing the frequency.

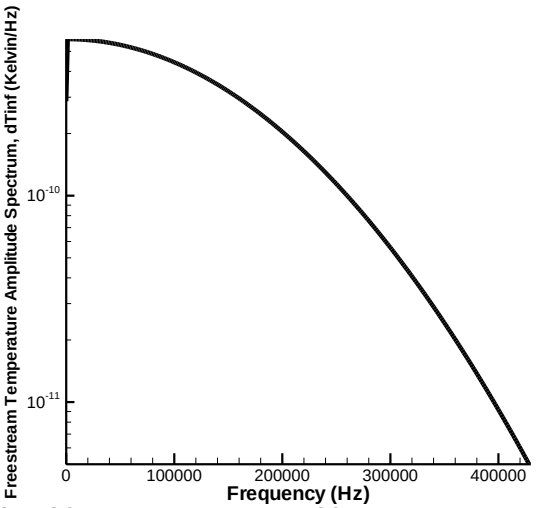

Figure 16. Dimensional frequency spectrum of freestream temperature perturbation.

Since the amplitude of the freestream forcing disturbance is not uniform in frequencies, it is necessary to normalize the wall pressure perturbation frequency spectrum in Figure 15 by the frequency spectrum of the freestream forcing disturbance. Due to the recorded wall perturbation is a pressure perturbation and the freestream forcing is a temperature disturbance, the normalization shall be done between two nondimensional quantities. Therefore, the normalization is

$$\text{normalized amplitude} = \frac{\left|dP_i / P_\infty\right|}{\left|dT_{\infty,i} / T_\infty\right|} \tag{21}$$

where the wall pressure perturbation is first normalized by the freestream pressure and the freestream temperature disturbance is normalized by the freestream temperature. Then, the nondimensional wall pressure perturbation amplitude is normalized by the nondimensional freestream temperature disturbance amplitude at each corresponding i^{th} frequency. The resulting normalized frequency spectrum is demonstrated in Figure 17. The normalized frequency spectrum reveals the relative growth of pressure perturbation to the freestream forcing disturbance at each frequency. Moreover, the normalized amplitude is analogous to "receptivity coefficient." It is a more accurate description of the instability growth. Since the boundary layer instability growth is linear, the normalized amplitude remains constant for this particular case of cone geometry and freestream flow conditions regardless of the freestream forcing wave. Hence, the nondimensional amplitude of a local instability spectrum at wall can be obtained linearly by multiplying the nondimensional amplitude of the freestream forcing spectrum to the normalized amplitude at each frequency. The normalized frequency spectrum in Figure 17 is a data library, which is built for this particular case of cone geometry and freestream flow conditions. It provides a convenience to avoid making another numerical simulation in order to obtain the results of local boundary layer instability for a different freestream forcing disturbance under the same freestream flow conditions and cone geometry.

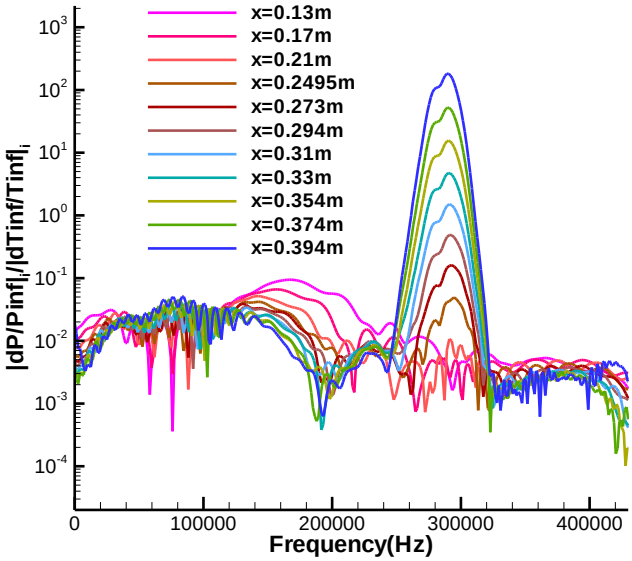

Figure 17. Non-dimensional frequency spectrum of wall pressure perturbation relative to freestream perturbation.

The normalized spectrum in Figure 17 seems slightly different to the spectrum in Figure 15. However, the wave observations that are made based on the normalized spectrum are basically the same as the dimensional spectrum in Figure 15. The normalized spectrum shows that there is a large spatially growing amplitude peak at the frequency range from about 260 kHz to 320 kHz. This largely growing peak is the second mode instability, which is verified in the latter part in this paper. The peak to the left of the growing peak, which is at the frequency range from 120 kHz to 240 kHz, decays spatially. This decaying peak could be the first mode wave at lower frequencies.

In order to validate the second mode growth in boundary layer, we carry out the LST analysis of the same freestream flow conditions. The LST analysis on the simulated mean flow is based on Lei et al.'s LST code [49]. There are five proposed frequencies that are within the LST predicted second mode frequency range: 257498 Hz, 271797 Hz, 278996 Hz, 292494 Hz and 297494 Hz. Since the LST proposed second mode frequency range overlaps with the dominantly growing peak frequency range, 260 kHz to 320 kHz, in numerical simulation, the dominantly growing peak is concluded to be the second mode instability. According to the LST N-factor result in Figure 18, the most amplified frequency amongst the five proposed ones is 278996 Hz, the second most amplified frequency is 292494 Hz, the third most amplified frequency is 271797 Hz, the fourth most amplified frequency is 297494 Hz for any location between $x = 0.25$ m to 0.4 m. The least amplified frequency is 257498 Hz for any location inside or outside of the range $x = 0.25$ m to 0.4 m.

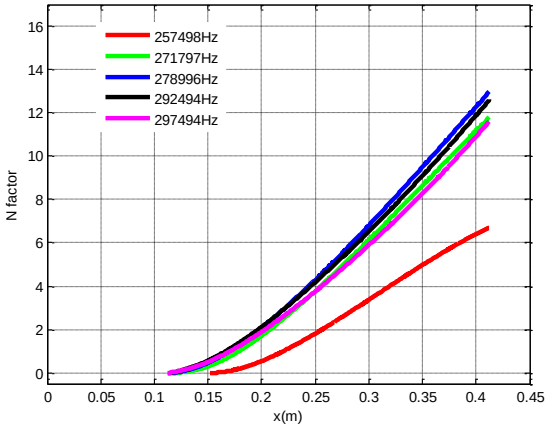

Figure 18. LST N-factor plot [13]

Figure 19 shows the development of the wall pressure perturbation amplitudes in the streamwise direction for the five sampling frequencies that are within the second mode frequency range from the numerical simulation. These five numerically simulated second mode sampling frequencies are the closest available sampling frequency to the five LST proposed frequencies. The amplitudes of the spectra are plotted in logarithmic scale in Figure 19. Between $x \approx 0.37$ m to 0.4 m, the most amplified sampling frequency is 293 kHz, the second most amplified sampling frequency is 280 kHz, the third most amplified sampling frequency is 297 kHz, the fourth most amplified sampling frequency is 272 kHz, and the least amplified frequency is 257 kHz. The five sampling second mode frequencies amplitudes start growing at $x \approx 0.2$ m. They grow linearly in tenth power. At the earlier locations in Figure 19, the oscillatory features of the curves are due to the existence of multi-wave-modes interactions, when the amplitude of the second mode wave is not dominant yet. The least amplified frequency from numerical simulation agrees with the LST N-factor results, but the order of the top four most amplified frequencies is different to the LST N-factor results. The main reason is due to the non-parallel and surface curvature effects that have not been included in the LST analysis.

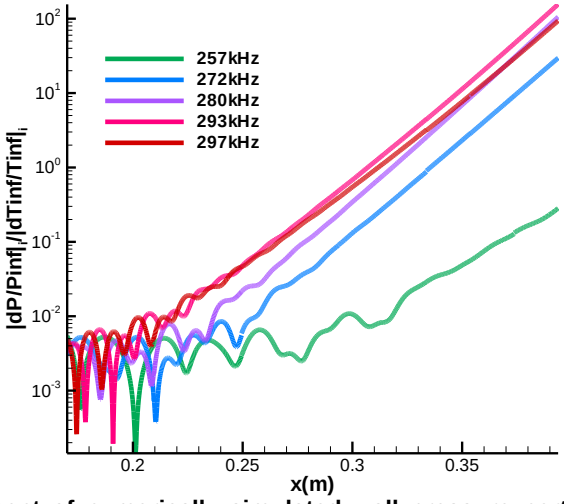

Figure 19. The spatial development of numerically simulated wall pressure perturbation at the five sampling frequencies in second mode frequency range.

The previous investigations focus on the instabilities at wall. The flow structures of the second mode instability in shock layer are demonstrated in Figure 20, the two-dimensional contour of the real Fourier component of the numerically simulated pressure perturbation at the most amplified frequency, 290 kHz, at the end of the cone. In the contour, the perturbation concentrates next to the wall, and the perturbation amplitude has spatial growth in downstream. There are almost no perturbation at this frequency exists far away from the wall.

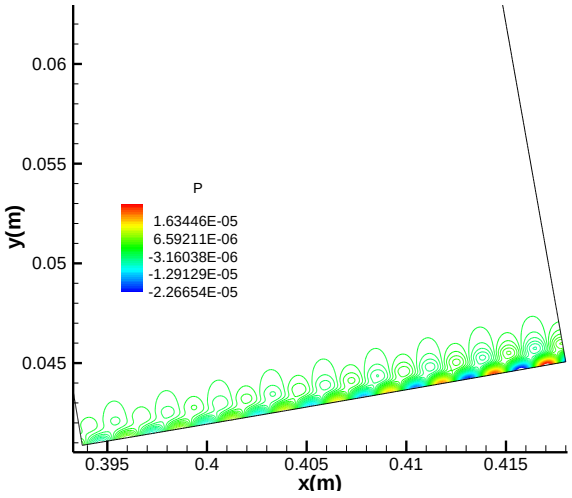

Figure 20. Two-dimensional contour of real component of Fourier transformed pressure perturbation at frequency of 290kHz from the numerical simulation. 'P' is pressure perturbation (Pa/Hz).

The previous comparison of the trend of the most amplified frequencies between numerically simulated results and the LST results is a qualitative aspect to see how close the numerically simulated results to the LST analysis are. In order to quantitatively validate the numerically simulated results with the LST results, the growth rates and wave numbers of the simulated wall pressure perturbation are computed according to equations (17) and (18). The comparisons between numerically simulated spatial growth rates and LST growth rates over the second mode instability frequency range at four downstream locations $x = 0.334\ \text{m}, 0.354\ \text{m}, 0.374\ \text{m}$, and $0.394\ \text{m}$ are demonstrated in Figure 21. The maximum relative difference between numerically simulated growth rates and LST growth rates are 16% at $x = 0.334\ \text{m}$, 13% at $x = 0.354\ \text{m}$, 11% at $x = 0.374\ \text{m}$, and 8% at $x = 0.394\ \text{m}$. The relative difference of growth rates consistently decrease while the sampling location moving downstream. At $x = 0.334\ \text{m}$, the frequency of the peak of numerically simulated growth rate is at 282 kHz, while the frequency of the peak of LST growth rate is at 284 kHz. At $x = 0.354\ \text{m}$, the frequency of the numerically simulated maximum growth rate is at 283.5 kHz, while the frequency of the maximum LST growth rate is at 284.5 kHz. At $x = 0.374\ \text{m}$, the frequency of the maximum numerically simulated growth rate is at 284 kHz, while the frequency of the maximum LST growth rate is at 286 kHz. At $x = 0.394\ \text{m}$, the frequency of the maximum numerically simulated growth rate is at 286 kHz, while the frequency of the maximum LST growth rate is at 287.5 kHz. The relative frequency differences at all four locations are below 1%, which indicate well comparisons between frequencies of the maximum simulated growth rates and the frequencies of the maximum LST growth rates. The reason for these differences to occur is likely due to the significance of non-parallel and surface curvature effects on LST analysis at upstream locations.

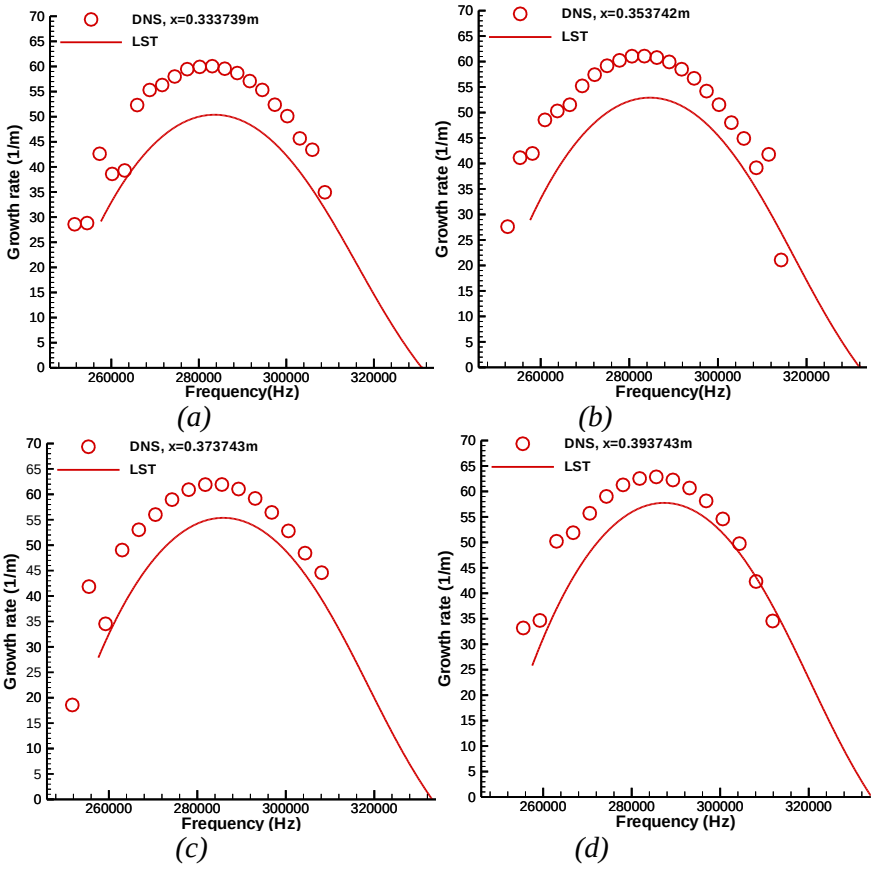

Figure 21. Comparisons of growth rate between numerical simulation and LST over second mode frequency range, (a) x = 0.334 m, (b) x = 0.354 m, (c) x = 0.374 m, and (d) x = 0.394 m.

The comparisons of the numerically simulated wave number and the LST wave number over the second mode instability frequency range at four downstream locations, $x = 0.334\ \text{m}, 0.354\ \text{m}, 0.374\ \text{m}$, and $0.394\ \text{m}$ are demonstrated in Figure 22. The maximum relative differences between numerically simulated wave numbers and LST wave numbers are 7.5% at $x = 0.334\ \text{m}$, 5.2% at $x = 0.354\ \text{m}$, 2.3% at $x = 0.374\ \text{m}$, and below 1% at $x = 0.394\ \text{m}$. The relative differences between LST and numerical simulation consistently decreases while the sampling location moving downstream. The reason for these differences to occur is likely due to the significance of non-parallel and surface curvature effects on LST analysis at upstream locations. However, the numerical wave numbers agree with LST wave numbers really well at downstream locations.

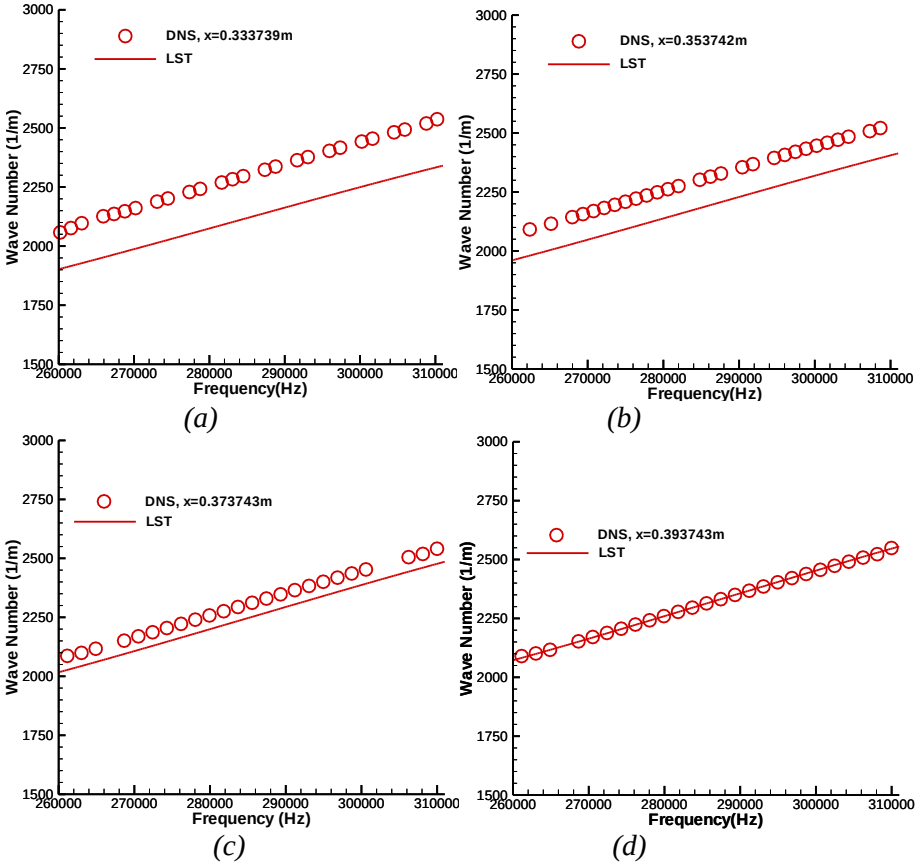

Figure 22. Comparisons of wave number between numerical simulation and LST over second mode frequency range, (a) x = 0.334 m, (b) x = 0.354 m, (c) x = 0.374 m, and (d) x = 0.394 m.

Figure 23 shows the comparison between the numerically simulated wall-normal boundary layer perturbation mode shape to the LST mode shape within boundary layer at the most amplified second mode sampling frequency of 292900 Hz. The comparison indicates high degree of agreement between numerically simulated mode shape and LST mode shape. From the above agreements from the three kinds of comparisons, it is concluded that the numerical simulation captures the linear development of hotspot boundary layer perturbation in a manner of high accuracy, and the resolution is sufficient.

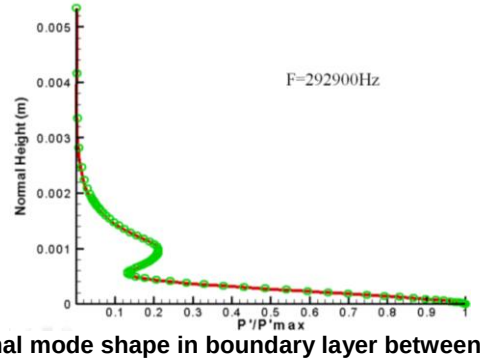

Figure 23. Comparisons of wall-normal mode shape in boundary layer between numerical simulation and LST for frequency of 292900 Hz at x = 0.311 m.

VII. Conclusions and Future Work

In conclusion from the receptivity analysis based on the unsteady flow simulation, introducing the interaction between freestream hotspot and bow-shock is an effective way to trigger second mode instability in boundary layer, which eventually leads to laminar-turbulent transition in downstream over a cone. The well-agreements between numerically simulated spectral results and LST results conclude that the numerical simulation captures the linear development of hotspot boundary layer perturbation in high accuracy, and the spatial and temporal resolutions are sufficient.

The main contribution of the hotspot receptivity study is to provide a data library of normalized spectrum with a wide range of frequencies for this particular freestream conditions and cone geometry. Thus, by scaling the normalized frequency spectrum with any freestream forcing spectrum, the amplitude of the wall perturbation can be computed without the hassle of performing another unsteady numerical simulation.

In the future, it will be interesting to investigate the three-dimensional development of hotspot in boundary layer by introducing a hotspot that impacts the shock without axisymmetry. It is also interesting to study the nonlinear effect of the hotspot to the boundary layer receptivity by introducing a hotspot with strong entropy core and a weak spherical shock wave that surrounds the entropy core. Such hotspot can be obtained by theoretical solutions such as Taylor's self-similar solution of a point explosion [51].

Acknowledgments

This work was sponsored by the AFOSR/NASA National Center for Hypersonic Research in Laminar-Turbulent Transition and by the Air Force Office of Scientific Research, USAF, under Grant No. FA9550-07-1-0414, monitored by Dr. John Schmisseur. The views and conclusions contained herein are those of the authors and should not be interpreted as necessarily representing the official policies or endorsements either expressed or implied, of the Air Force Office of Scientific Research or the U.S. Government. The authors of this paper specially thank to Professor Steven P. Schneider in Purdue University and his group for providing the data and information of their compression cone and other wind-tunnel experiments, which make the authors' work more comparable to the real-world experiments. The first author of this paper would like to thank Jia Lei in University of California, Los Angeles, for providing assistance in LST analysis.

References

[1] Dunn, J.W., "Numerical Simulation of Bow-Shock/Disturbance Interactions in Mach-4 Flows Past a Hemisphere" AIAA Paper, 98-0007, January 1998.

[2] Reshotko E., "Hypersonic Stability and Transition", Hypersonic Flows for Reentry Problems, Berlin: Springer, 1991.

[3] Salyer, T.R., "Laser Differential Interferometry for Supersonic Blunt Body Receptivity Experiments", PhD Thesis, Purdue University, May 2002.

[4] Salyer, T.R., Collicott, S.H., Schneider, S.P., "Characterizing Laser-Generated Hot Spots for Receptivity Studies", AIAA Journal, Vol.44, No.12, December 2006.

[5] Wheaton, B.M., Julinao, T.J., Berridge, D.C., Chou, A., Gilbert P.L., Casper. K.M., Steen, L.E., Schneider, S.P., "Instability and Transition Measurements in the Mach-6 Quiet Tunnel", AIAA Paper, 2009-3559, June 2009.

[6] Zhong, X., "High-Order Finite-Difference Schemes for Numerical Simulation of Hypersonic Boundary-Layer Transition", Journal of Computational Physics 144,662-709, April 1998.

[7] Zhong, X., "Receptivity of Mach 6 Flow over a Flared Cone to Freestream Disturbance", AIAA Paper, 2004-253, January 2004.

[8] Zhong, X., Lee, T.K., "Nonequilibrium Real-Gas Effects on Disturbance/Bow Shock Interaction in Hypersonic Flow Past a Cylinder", AIAA, 1996.

[9] Schmisseur, J.D., Collicott, S.H., Schneider, S.P., "Laser-Generated Localized Freestream Perturbations in Supersonic and Hypersonic Flows", AIAA Journal, vol. 38, No.4, April 2000.

[10] McKenzie, J. F., Westphal, K. O., "Interaction of Linear Waves with Oblique Shock Waves", The Physics of Fluids, Vol. 11, No. 11, November 1968.

[11] Kovasznay, L. S. G., "Turbulence in Supersonic Flow", Journal of the Aeronautical Sciences, Vol. 20, No. 10, pp. 657-682, October 1953.

[12] Malik, M. R., "Numerical Method for Hypersonic Boundary Layer Stability", Journal of Computational Physics, 86, 376-413, 1990.

[13] Huang, Y., Zhong, X., "Numerical Study of Laser-Spot Effects on Boundary-Layer Receptivity for Blunt Compression-Cones in Mach-6 Freestream", AIAA paper, 2010-4447, June 2010.

[14] Ward, C.A.C., Wheaton, B.M., Chou, A., Gilbert, P.L., Steen, L.E., Schneider, S.P., "Boundary-Layer Transition Measurements in a Mach-6 Quiet Tunnel", AIAA paper, 2010-4721, June 2010.

[15] Chou, A., "Characterization of Laser-Generated Perturbations and Instability Measurements on a Flared Cone", MS Thesis, Purdue University, December 2010.

[16] Ma, Y., Zhong, X., "Receptivity of a Supersonic Boundary Layer over a Flat Plate. Part 3. Effects of Different Types of Free-stream Disturbances", Journal of Fluid Mechanics, vol. 532, pp. 63-109. December 2004.

[17] Pruett, C.D., Chang, C.L., "Direct Numerical Simulation of Hypersonic Boundary-Layer Flow on a Flared Cone", Theoretical and Computational Fluid Dynamics (1998) 11:49-67, Springer-Verlag 1998.

[18] Balakumar, P., Kegerise, M.A., "Receptivity of Hypersonic Boundary Layers over Straight and Flared Cones", AIAA paper, 2010-1065, January 2010.

[19] Mack, L.M., "Boundary Layer Linear Stability Theory", AGARD report, No. 709, pp.3-1 to 3-81, 1984.

[20] Press W.H., Flannery, B.P., Teukolsky, S.A., Vetterling, W.T., "Numerical Recipes", Cambridge University Press 1986.

[21] Sivasubramanian, J., Fasel, H.F. "Numerical Investigation of Boundary-layer Transition Initiated by a Wave Packet for a Cone at Mach 6", AIAA paper, 2010-900, January 2010.

[22] Randall, L.A., "Receptivity Experiments on a Hemispherical Nose at Mach 4", M.S. Thesis, School of Aeronautics and Astronautics, Purdue Univ., W. Lafayette, IN, 1996.

[23] Stetson, K.F., Thompson, E.R., Donaldson, J.C., Siler, L.G., "Laminar Boundary Layer Stability Experiments on a Cone at Mach 8, Part 2: Blunt Cone", AIAA paper, 84-0006, January 1984.

[24] Sivasubramanian, J., Mayer, C.S.J., Laible, A.C., Fasel, H.F., "Numerical Investigation of Wavepackets in a Hypersonic Cone Boundary Layer at Mach 6", AIAA paper, 2009-3560, June 2009.

[25] Sivasubramanian, J., Fasel, H.F., "Direct Numerical Simulation of a Turbulent Spot in a Cone Boundary-Layer at Mach 6", AIAA paper, 2010-4599, June 2010.

[26] Sivasubramanian, J., Fasel, H.F., "Transition Initiated by a Localized Disturbance in a Hypersonic Flat-Plate Boundary Layer", AIAA paper, 2011-374, January 2011.

[27] Salyer, T.R., Collicott, S.H., Schneider, S.P., "Feedback Stabilized Laser Differential Interferometry for Supersonic Blunt Body Receptivity Experiments", AIAA paper, 2000-0416, January 2000.

[28] Ladoon, D.W., Schneider, S.P., Schmisseur, J.D., "Physics of Resonance in a Supersonic Forward-Facing-Cavity", Journal of Spacecraft and Rockets, vol. 35, No. 5, September-October 1998.

[29] Chou, A., Wheaton, B.M., Ward, C.A.C., Gilbert, P.L., Steen, L.E., Schneider, S.P., "Instability and Transition Research in a Mach-6 Quiet Tunnel", AIAA paper, 2011-283, January 2011.

[30] Schneider, S.P., Collicott, S.H., "Laminar-Turbulent Transition in High-Speed Compressible Boundary Layers: Continuation of Elliptic-Cone Experiments", Final Report, School of Aeronautical and Astronautical Engineering, Purdue Univ. W. Lafayette, IN, January 2000.

[31] Casper, K.M., Beresh, S.J., Schneider, S.P., "Pressure Fluctuations beneath Turbulent Spots and Instability Wave Packets in a Hypersonic Boundary Layer", AIAA paper, 2011-372, January 2011.

[32] Schmisseur, J.D., "Receptivity of the Boundary Layer on a Mach 4 Elliptic Cone to Laser-Generated Localized Free Stream Perturbations", PhD Thesis, Purdue Univ., W. Lafayette, IN, December 1997.

[33] Heitmann, D., Kahler, C.J., Radespiel, R., "Installation of a System for Laser-Generated Perturbations in Hypersonic Flow", 14th International Symposium on Application of Laser Techniques to Fluid Mechanics, July 2008.

[34] Heitmann, D., Kahler, C.J., Radespiel, R., "Investigation of Laser Generated Perturbations for Boundary Layer Stability Experiments", Numerical & Experimental Fluid Mechanics VII, NNFM 1112, pp. 297-305, Springer-Verlag Berlin Heidelberg 2010.

[35] Heitmann, D., Kahler, C.J., Radespiel, R., Rodiger, T., Knauss, H., Wagner, S., "Non-Intrusive Generation of Instability Waves in a Planar Hypersonic Boundary Layer", Exp Fluids, 50:457-464, Springer-Verlag 2010.

[36] Heitmann, D., Radespiel, R., Kahler, C.J., "Investigation of the Response of a Hypersonic 2D Boundary Layer to Controlled Acoustic Disturbances", AIAA paper, 2010-536, January 2010.

[37] Heitmann, D., Kahler, C.J., Radespiel, R., "Investigation of Laser-Generated Flow Perturbations in

Hypersonic Flow over a Flat Plate", AIAA paper, 2008-3737, June 2008.

[38] Huang, Y., Zhong, X., " Numerical Study of Freestream Hot-Spot Perturbation on Boundary-Layer Receptivity for Blunt
Compression-Cones in Mach-6 Flow", AIAA paper, 2011-3078, June 2011.

[39] Sivasubramanian, J., Fasel, H., "Numerical Investigation of Laminar-Turbulent Transition in a Cone Boundary Layer at
Mach 6", AIAA paper, 2011-3562, June 2011.

[40] Laible, A., Fasel, H., "Numerical Investigation of Hypersonic Transition for a Flared and a Straight Cone at Mach 6", AIAA
paper, 2011-3565, June 2011.

[41] Heitmann, D., Radespiel, R., "Simulation of the Interaction of a Laser Generated Shock Wave with a Hypersonic Conical
Boundary Layer", AIAA paper, 2011-3875, June 2011.

[42] Heitmann, D., Radespiel, R., Knauss, H., "Experimental Study of Mach 6 Boundary Layer Response to Laser Generated
Disturbances", AIAA paper, 2011-3876, June 2011.

[43] Fedorov, V. A., Ryzhov, A. A., Soudakov, G. V., "Numerical and Theoretical Modeling of Supersonic Boundary-Layer
Receptivity to Temperature Spottiness", AIAA paper, 2011-3077, June 2011.

[44] Zhong, X., Ma, Y., "Boundary-Layer Receptivity of Mach 7.99 Flow over a Blunt Cone to Free-Stream Acoustic Waves", Journal of Fluid Mechanics, vol. 556, pp. 55-103, May 2006.

[45] Fedorov, V. A., "Receptivity of a high-speed boundary layer to acoustic disturbances", Journal of Fluid Mechanics, vol. 491, pp 101-129, August 2003.

[46] Maslov, A. A., Shiplyuk, A. N., Sidorenko, A. A., and Arnal, D., "Leading-Edge Receptivity of a Hypersonic Boundary Layer on a Flat Plate", Journal of Fluid Mechanics, vol. 426 , pp 73-94, January 2001.

[47] Johnson, H. B., and Candler, G. V., "Analysis of Laminar-Turbulent Transition in Hypersonic Flight
Using PSE-Chem", AIAA paper, 2006-3057, June 2006.

[48] Hofferth, J., and Saric, W., "Boundary-Layer Transition on a Flared Cone in a Mach 6 Quiet Wind Tunnel", American Physical Society, 63rd Annual Meeting of the APS Division of Fluid Dynamics, November 21-23, 2010, abstract #CE.004

[49] Lei, J., Zhong, X., "Linear Stability Analysis of Nose Bluntness Effects on Hypersonic Boundary Layer Transition", AIAA paper, 2010-0898, January 2010.

[50] Stetson, K.F., Thompson, E. R., Donaldson, J. C., and Siler, L. G., " Laminar Boundary Layer Stability Experiments on a Cone at Mach 8, Part 2: Blunt Cone", AIAA paper, 84-0006, 1984.

[51] Taylor, G., "The Formation of a Blast Wave by a Very Intense Explosion. I. Theoretical Discussion", Proceedings of the Royal Society of London. Series A, Mathematical and Physical Sciences, Vol. 201, No. 1065, pp. 159-174, March 1950.